International Journal of Extreme Manufacturing

A combined multiscale modeling and experimental study on surface modification of high-volume micro-nanoparticles with atomic accuracy

OPEN ACCESS
IOP Publishing | IMMT
International Journal of Extreme Manufacturing
Int. J. Extrem. Manuf. 4 (2022) 025101 (16pp)
https://doi.org/10.1088/2631-7990/ac529c

A combined multiscale modeling and experimental study on surface modification of high-volume micro-nanoparticles with atomic accuracy

Zoushuang Li[1], Junren Xiang[1,5], Xiao Liu[1], Xiaobo Li[2], Lijie Li[3], Bin Shan[4] and Rong Chen[1,*]

[1] State Key Laboratory of Digital Manufacturing Equipment and Technology, School of Mechanical Science and Engineering, Huazhong University of Science and Technology, 1037 Luoyu Road, Wuhan, Hubei 430074, People's Republic of China
[2] School of Energy and Power Engineering, Huazhong University of Science and Technology, Wuhan, Hubei 430074, People's Republic of China
[3] College of Engineering, Swansea University, SA1 8EN Swansea, United Kingdom
[4] State Key Laboratory of Material Processing and Die and Mould Technology, School of Materials Science and Engineering, Huazhong University of Science and Technology, Wuhan, Hubei 430074, People's Republic of China
[5] Wuhan University of Technology, Wuhan, Hubei 430063, People's Republic of China

E-mail: rongchen@mail.hust.edu.cn

Received 15 October 2021, revised 8 December 2021
Accepted for publication 7 February 2022
Published 23 February 2022

Abstract

Surface modification for micro-nanoparticles at the atomic and close-to-atomic scales is of great importance to enhance their performance in various applications, including high-volume battery, persistent luminescence, etc. Fluidized bed atomic layer deposition (FB-ALD) is a promising atomic-scale manufacturing technology that offers ultrathin films on large amounts of particulate materials. Nevertheless, nanoparticles tend to agglomerate due to the strong cohesive forces, which is much unfavorable to the film conformality and also hinders their real applications. In this paper, the particle fluidization process in an ultrasonic vibration-assisted FB-ALD reactor is numerically investigated from micro-scale to macro-scale through the multiscale computational fluid dynamics and discrete element method (CFD-DEM) modeling with experimental verification. Various vibration amplitudes and frequencies are investigated in terms of their effects on the fluid dynamics, distribution of particle velocity and solid volume fraction, as well as the size of agglomerates. Results show that the fluid turbulent kinetic energy, which is the key power source for the particles to obtain the kinetic energy for overcoming the interparticle agglomeration forces, can be strengthened obviously by the ultrasonic vibration. Besides, the application of ultrasonic vibration is found to reduce the mean

* Author to whom any correspondence should be addressed.

2631-7990/22/025101+16$33.00

agglomerate size in the FB. This is bound to facilitate the heat transfer and precursor diffusion in the entire FB-ALD reactor and the agglomerates, which can largely shorten the coating time and improve the film conformality as well as precursor utilization. The simulation results also agree well with our battery experimental results, verifying the validity of the multiscale CFD-DEM model. This work has provided momentous guidance to the mass manufacturing of atomic-scale particle coating from lab-scale to industrial applications.

Keywords: atomic scale manufacturing, fluidized bed atomic layer deposition (FB-ALD), computational fluid dynamics and discrete element method (CFD-DEM), nanoparticle agglomerates, ultrasonic vibration

1. Introduction

Surface modification of micro-nanoparticles at the atomic and close-to-atomic scales is of great importance to their applications in a variety of fields, such as energy storage [1–3], catalysis [4, 5], sensors [6], biomedicine [7, 8], etc. In order to meet the industry requirements in these areas, it is urgently necessary to develop high-volume manufacturing of atomically precise coatings on particulate materials. As an advanced extreme manufacturing method, atomic layer deposition (ALD) is a thin film deposition method which offers pinhole-free films with precise thickness control at the angstrom level and exceptional homogeneity on complex structures [9, 10]. Fluidized bed ALD (FB-ALD) has shown great potential in atomically ultrathin films on large amounts of particles [11, 12].

However, with the surface area of nanoparticles increasing dramatically in scale-up manufacturing, challenges for FB-ALD begin to exist. High surface energy and strong cohesive forces between nanoparticles can cause severe aggregation, leading to the formation of micro-sized agglomerates and fluidization problems, such as channeling, bubbling, clustering, and elutriation [13–15]. Large agglomerates cause the decrease of exposed nanoparticle surface area and increase in heat and mass resistances, leading to the non-uniformity of nanoparticle coating and a long coating time [16]. Besides, precursor molecules might be directly purged out before being fully consumed by the active sites on particle surfaces, leading to a low precursor utilization. Enhancing the fluidization quality of nanoparticles is of great importance to improve the efficiency of FB-ALD, especially for the scalable production of nanoparticle coatings [17, 18].

In the past few decades, different external assisting methods have been proposed to enhance the fluidization quality in FB-ALD reactors, such as mechanical vibration [19], agitation [20], pulsation [21], and rotation [22]. Experimental results showed that these external forces could effectively facilitate the breakage of agglomerates and the gas–solid mixing [23]. In addition, as an indicator of the fluidization quality, the hydrodynamics in the FB-ALD reactor assisted with external forces is also improved, such as higher bed expansion ratio and lower minimum fluidization velocity. Due to these improvements, the film conformality and the precursor utilization are both effectively enhanced [24].

Despite various experimental investigations, a comprehensive understanding of the external field effects on the FB-ALD process is still required. FB-ALD is a strong-coupled multiscale process, where the fluid dynamics at the reactor scale (∼s) is combined with diffusion in the micro-sized agglomerates (∼ms) and ALD reaction kinetics (∼μs) at the atomic scale [16, 25]. As a consequence, establishing a precise model to simultaneously investigate the behaviors under different length and time scales for the fluid-particle system is extremely complicated [26]. Whereas, since the fluidization quality makes a great difference to the FB-ALD coating process, the numerical simulation on nanoparticle fluidization behaviors is a great alternative. At the reactor and agglomerate scales, computational fluid dynamics (CFD) is the most widely used approach to explore the hydrodynamics of gas–solid flow [27, 28]. Depending on whether the particles are treated as a continuum phase or discrete phase, CFD methods can be categorized into Eulerian–Eulerian and Eulerian–Lagrangian models [29–31]. Using the Eulerian–Eulerian method, Rossbach *et al* investigated the effect of ultrasonic waves on micro-sized particle fluidization in a circulating FB riser [32, 33]. Both the numerical and experimental results showed that ultrasound waves enhanced the distribution of solid particles, and a better fluidization quality was obtained with an acoustic frequency of 20 kHz and input power from 10 W to 50 W. As for the Eulerian–Lagrangian approach, particles are modeled individually by a discrete element method (DEM) [34–36]. In this way, the particle-to-particle and particle-to-fluid interactions can be simultaneously considered rationally. Using the CFD-DEM method, Tang *et al* investigated the effects of the acoustic fields on the agglomeration behavior of cohesive micro-sized particles [37]. Results showed that the application of acoustic field promoted the breakup of agglomerates, leading to a remarkable improvement of the process performance. As a source of high-frequency sound waves, ultrasonic vibration has also been proved to increase the heat and mass transfer rates and promote chemical reactions [38, 39]. Nevertheless, the application of ultrasonic vibration on the low-pressure FB-ALD process hasn't been reported yet, neither CFD-DEM simulations for the effect of ultrasonic waves on nanoparticle fluidization.

The schematic of the ultrasonic vibration-assisted FB-ALD process is shown in figure 1. As is shown, nanoparticles are fluidized as micro-sized agglomerates in the FB due to the cohesive forces between the agglomerates, such as van der Waals force, liquid-bridge force, and electrostatic force [40]. The separation forces between the agglomerates include

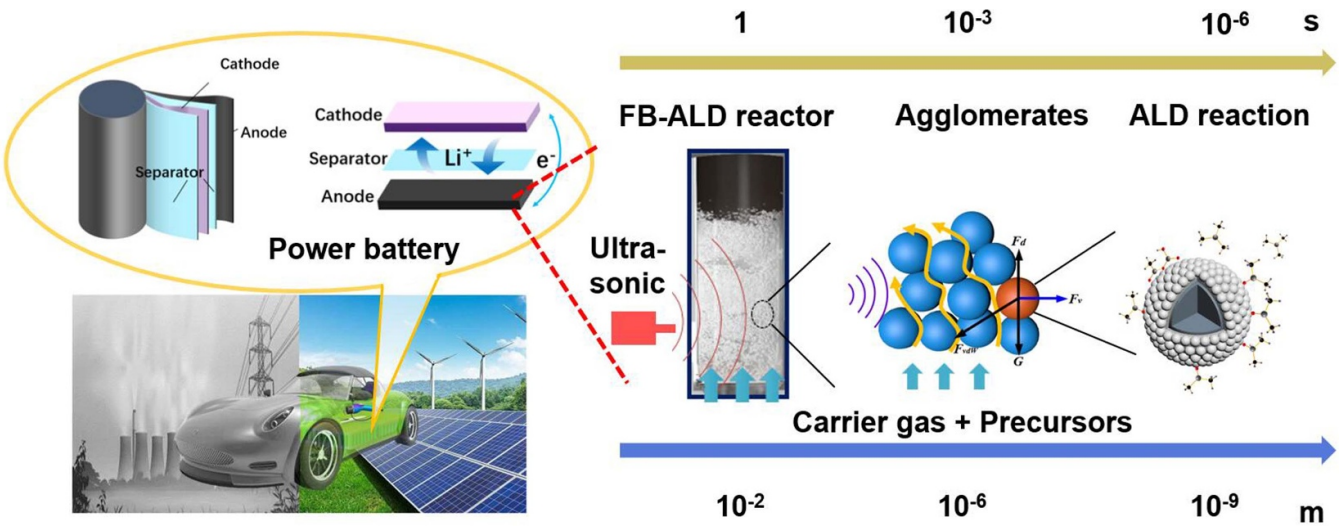

Figure 1. Nanoparticle application in power batteries for electric vehicles and the schematic of the ultrasonic vibration-assisted FB-ALD process.

particle–wall, particle–particle collision forces, particle–fluid drag force, and gravity force. Ultrasonic waves are induced by the vibrating motion of the FB sidewall, which is activated by ultrasonic horns or transducers. The ultrasonic vibration causes increased particle–wall collisions as well as periodic disturbance to the flow field in the FB-ALD reactor. After reaching a stable fluidization state, precursors are successively pulsed into the reactor to achieve ALD reaction on nanoparticle surfaces, typically being trimethyl-aluminum (TMA) and H_2O for Al_2O_3 films. It is noted that hydrodynamics in the ultrasonic vibration-assisted FB-ALD reactor not only has an impact on the agglomeration behavior but also affects the mass and heat transfer rates in the reactor or agglomerates.

Towards the large-scale manufacturing of atomically thin coatings on nanoparticles, this work aims to investigate the effect of ultrasonic vibration on the hydrodynamics and the particle agglomeration behavior in an FB-ALD reactor via CFD-DEM simulation. The dynamic mesh method is adopted to reveal the ultrasonic vibration of the FB sidewall, and the Johnson–Kendall–Roberts (JKR) model is applied to simulate the cohesive forces between agglomerates. For forces acting on particles, the particle–particle, and particle–wall collision forces, particle–fluid interactions are considered. The bed pressure drops and expansions, fluid turbulent kinetic energy, distribution of particle velocities and solid volume fraction, as well as the agglomerate sizes are presented to characterize the fluidization quality. Different amplitudes and frequencies of ultrasonic vibrations are investigated to find the optimal conditions for enhancing the fluidization quality and the coating efficiency of FB-ALD process.

2. Numerical methodology

In this study, the effects of ultrasonic vibration on the hydrodynamics at the reactor scale and the particle agglomeration behavior at the agglomerate scale are numerically investigated through the Eulerian–Lagrangian simulation. The gas phase is considered as a continuous phase by solving the Navier–Stokes equations, and the particle agglomerates are tracked individually through Newton's equation of motion. Several assumptions are made for the simplification of calculation. Firstly, simple nanoparticle agglomerates are treated as spherical DEM particles with the same properties. Secondly, the ultrasonic vibration with constant amplitude and frequency is applied to part of the FB sidewall. Therefore, the attenuation of the ultrasonic energy hasn't been taken into consideration, as well as the propagation and reflection of ultrasonic waves in solid structures. Thirdly, the FB is considered isothermal, and mass transfer between phases is neglected.

2.1. Hydrodynamics of gas phase

The motion of the gas phase can be modeled using Euler's equations. According to the Navier–Stokes equations, the mass conservation equation for the gas phase is described as:

$$\frac{\partial}{\partial t}\left(\alpha_{\mathrm{g}}\rho_{\mathrm{g}}\right)+\nabla\left(\alpha_{\mathrm{g}}\rho_{\mathrm{g}}\overrightarrow{v_{\mathrm{g}}}\right)=0 \tag{1}$$

where α_{g} is the local volume fraction of fluid, and $\overrightarrow{v_{\mathrm{g}}}$ represents the gas velocity. ρ_{g} is the fluid density, which is calculated based on the ideal gas law:

$$\rho_{\mathrm{g}}=\frac{p}{RT} \tag{2}$$

where p is the gas pressure, R is the ideal gas constant of nitrogen with the value of 2969 J $(\mathrm{kg{\cdot}K})^{-1}$, and T is the gas temperature with the value of 423 K. The conservation equation of momentum for the gas phase can be written as:

$$\frac{\partial}{\partial t}\left(\alpha_{\mathrm{g}}\rho_{\mathrm{g}}\overrightarrow{v_{\mathrm{g}}}\right)+\nabla\left(\alpha_{\mathrm{g}}\rho_{\mathrm{g}}\overrightarrow{v_{\mathrm{g}}}\overrightarrow{v_{\mathrm{g}}}\right)=-\alpha_{\mathrm{f}}\nabla p+\nabla\cdot\overline{\overline{\tau}}_{\mathrm{g}}+\alpha_{\mathrm{g}}\rho_{\mathrm{g}}\vec{g}+\vec{S} \tag{3}$$

where $\overline{\overline{\tau}}_g$ is the fluid phase stress–strain tensor:

$$\overline{\overline{\tau}}_g = \alpha_g \mu_g \left(\nabla \vec{v}_g + \nabla \vec{v}_g^{\mathrm{T}}\right) + \alpha_g \left(\lambda_g - \frac{2}{3}\mu_g\right) \nabla \cdot \vec{v}_g \overline{\overline{I}} \quad (4)$$

where μ_g and λ_g are the shear and bulk viscosity of the gas phase, respectively. $\overline{\overline{I}}$ is the intensity of turbulent kinetic energy. $\vec{S}$ is the volumetric gas–particle interaction force in a computational cell, which is given by:

$$\vec{S} = \frac{\sum_{i=1}^{N} f_{pg,i}}{V_c} \quad (5)$$

where N is the number of particles, $f_{pg,i}$ is the fluid force acting on the ith particle, and V_c is the volume of the cell.

The turbulent flow in the ultrasonic vibration-assisted FB is modeled by the standard $k-\varepsilon$ dispersed turbulence model. The transport equations of turbulence kinetic energy, k, and the rate of dissipation, ε, are as follows:

$$\frac{\partial}{\partial t}(\alpha_g \rho_g k) + \nabla \cdot \left(\alpha_g \rho_g \overrightarrow{v_g} k\right) = \nabla \cdot \left(\alpha_g \left(\mu_g + \frac{\mu_t}{\sigma_k}\right) \nabla k\right) + \alpha_g G_k - \alpha_g \rho_g \varepsilon \quad (6)$$

$$\frac{\partial}{\partial t}(\alpha_g \rho_g \varepsilon) + \nabla \cdot \left(\alpha_g \rho_g \overrightarrow{v_g} \varepsilon\right) = \nabla \cdot \left(\alpha_g \left(\mu_g + \frac{\mu_t}{\sigma_k}\right) \nabla k\right) + \alpha_g \frac{\varepsilon}{k}\left(C_1 G_k - C_2 \rho_g \varepsilon\right) \quad (7)$$

where G_k represents the generation of turbulence kinetic energy due to mean velocity gradients. σ_k and σ_ε are the turbulent Prandtl numbers for k and ε. μ_t is the turbulent viscosity, and it is calculated by:

$$\mu_t = \rho_g C_\mu \frac{k^2}{\varepsilon} \quad (8)$$

where C_1, C_2, and C_μ are the model constants with the empirical values of 1.44, 1.92, and 0.09, respectively.

2.2. DEM of particle motions

In the Euler–Lagrangian model, the fluidizing particles are simplified as spherical particles with the same properties. The forces acting on the particles include gravity force, particle–wall and particle–particle contact forces, as well as the interaction forces between particles and the gas phase. According to Newton's second law, the governing equations for the motion of particle i can be written as:

$$m_i \frac{\mathrm{d}\overrightarrow{v_i}}{\mathrm{d}t} = \sum_{j=1}^{N}\left(\overrightarrow{F_{cnij}} + \overrightarrow{F_{ctij}} + \overrightarrow{F_{dnij}} + \overrightarrow{F_{dtij}}\right) + \overrightarrow{F_{d,\,gi}} + \overrightarrow{F_{p,\,gi}} + m_i \vec{g} \quad (9)$$

$$I_i \frac{\mathrm{d}\overrightarrow{w_i}}{\mathrm{d}t} = \sum_{j=1}^{N} \overrightarrow{T_{ij}} \quad (10)$$

where m_i, I_i, $\overrightarrow{v_i}$, and $\overrightarrow{w_i}$ represents the mass, moment of inertia, linear velocity, and angular velocity of particle i, respectively. $\overrightarrow{F_{cnij}}$, $\overrightarrow{F_{ctij}}$, $\overrightarrow{F_{dnij}}$, and $\overrightarrow{F_{dtij}}$ are the normal contact force, tangential contact force, normal damping force, and tangential damping force between particle i and j that act on particle i. N is the number of particles in contact with particle i. $\overrightarrow{F_{d,\,gi}}$ and $\overrightarrow{F_{p,\,gi}}$ are the gas–particle drag force and pressure force acting on particle i, accordingly. $\overrightarrow{T_{ij}}$ is the torques that particle j acting on particle i.

For the consideration of cohesive forces between particles, Hertz–Mindlin with JKR cohesion model is adopted to calculate the contact forces between particles [41]. According to Hertz–Mindlin contact theory and JKR theory, the $\overrightarrow{F_{cnij}}$, $\overrightarrow{F_{ctij}}$, $\overrightarrow{F_{dnij}}$, and $\overrightarrow{F_{dtij}}$ between particles can be calculated as follows:

$$\overrightarrow{F_{cnij}} = -4\sqrt{\pi\gamma E^*}\alpha^{\frac{3}{2}} + \frac{4E^*}{3R^*}\alpha^3 \quad (11)$$

$$\overrightarrow{F_{ctij}} = S_t \delta_t \quad (12)$$

$$\overrightarrow{F_{dnij}} = -2\sqrt{\frac{5}{6}}\frac{\ln e\sqrt{S_n m^*}\overrightarrow{v_n^{rel}}}{\sqrt{\ln^2 e + \pi^2}} \quad (13)$$

$$\overrightarrow{F_{dtij}} = -2\sqrt{\frac{5}{6}}\frac{\ln e\sqrt{S_t m^*}\overrightarrow{v_t^{rel}}}{\sqrt{\ln^2 e + \pi^2}} \quad (14)$$

where γ is the surface energy of particles, which is set as 0.04 mJ m^{-2}, based on the assumption that the maximum cohesive force is equal to 20 times of the gravity force. δ_t represents tangential overlap distance. $\overrightarrow{v_n^{rel}}$ and $\overrightarrow{v_t^{rel}}$ are the normal and tangential components of the relative velocity. S_n and S_t are normal and tangential stiffness, which is calculated by:

$$S_n = 2E^*\sqrt{R * \delta_n} \quad (15)$$

$$S_t = 8G^*\sqrt{R^*\delta_n}. \quad (16)$$

The relationship between α and normal overlap distance δ_n can be described as:

$$\delta_n = \frac{\alpha^2}{R^*} - \sqrt{\frac{4\pi\gamma\alpha}{E^*}}. \quad (17)$$

E^*, R^* and m^* are the equivalent Young's modulus, radius and mass, which can be represented by:

$$\frac{1}{E} = \frac{\left(1-v_i^2\right)}{E_i} + \frac{\left(1-v_j^2\right)}{E_j} \quad (18)$$

$$\frac{1}{R^*} = \frac{1}{R_i} + \frac{1}{R_j} \quad (19)$$

$$\frac{1}{m^*} = \frac{1}{m_i} + \frac{1}{m_j} \quad (20)$$

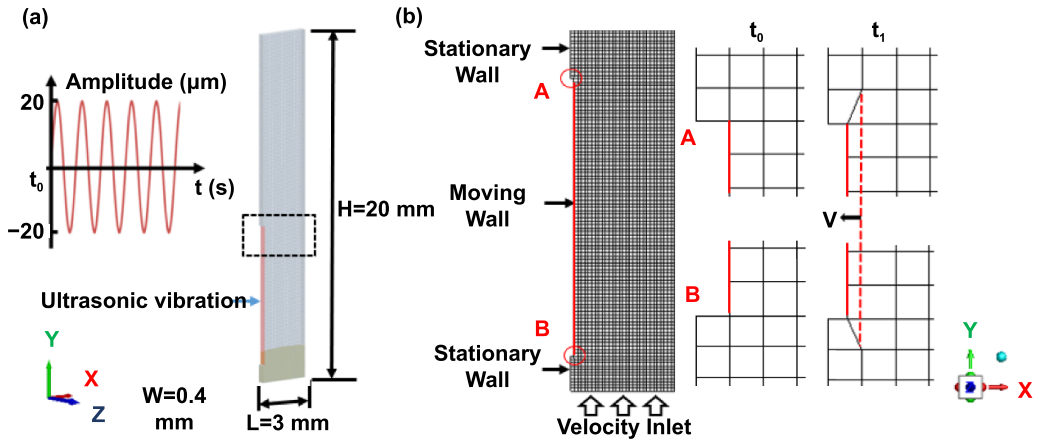

Figure 2. (a) Pseudo-2D geometry model and boundary conditions of ultrasonic vibration-assisted FB-ALD reactor; (b) enlarged view for the setup of dynamic mesh in the fluid computational domain.

where E_i, E_j, R_i, R_j, v_i, v_j, and m_i, m_j are Young's modulus, Poisson ratio, radius, and mass of particle i and j.

The cohesive force between particles and walls is neglected. Therefore, the Hertz–Mindlin model is used to calculate the contact force between particles and walls, where γ is assigned to zero. Besides, in particle–wall collisions, the mass of particle j (the wall) is set infinitely large, leading to $m^* = m_i$.

The drag force is calculated by:

$$\overrightarrow{F_{\mathrm{d},\,gi}} = \frac{V_\mathrm{P}\beta}{1-\varepsilon_\mathrm{g}}\left(\vec{v}_\mathrm{g} - \vec{v}_\mathrm{p}\right) \tag{21}$$

where ε_g is the gas volume fraction, V_P is the particle volume, and β is the fluid-particle drag coefficient. The well-known Gidaspow model is employed for the correlations of β:

$$\beta = \begin{cases} 150\dfrac{(1-\varepsilon_\mathrm{g})^2\mu_\mathrm{g}}{\varepsilon_\mathrm{g}{d_\mathrm{p}}^2} + 1.75\dfrac{\rho_\mathrm{g}(1-\varepsilon_\mathrm{g})\left|\vec{v}_\mathrm{g}-\vec{v}_\mathrm{p}\right|}{d_\mathrm{p}} & \varepsilon_\mathrm{g} < 0.8 \\ \dfrac{3}{4}C_\mathrm{d}\dfrac{\rho_\mathrm{g}(1-\varepsilon_\mathrm{g})\left|\vec{v}_\mathrm{g}-\vec{v}_\mathrm{p}\right|}{d_\mathrm{p}}\varepsilon_\mathrm{g}^{-2.65} & \varepsilon_\mathrm{g} \geqslant 0.8 \end{cases} \tag{22}$$

where d_p is the particle diameter and C_d is the drag coefficient following the Schiller and Naumann correlation:

$$\mathrm{C_d} = \begin{cases} \dfrac{24}{\mathrm{Re}}\left(1+0.15\mathrm{Re}^{0.687}\right) & \mathrm{Re} < 1000 \\ 0.44 & \mathrm{Re} \geqslant 1000 \end{cases}. \tag{23}$$

The Reynolds number, Re, is defined by:

$$\mathrm{Re} = \frac{\rho_\mathrm{g}\varepsilon_\mathrm{g}d_\mathrm{p}\left|\vec{v}_\mathrm{g}-\vec{v}_\mathrm{p}\right|}{\mu_\mathrm{g}}. \tag{24}$$

The pressure force acting on a single particle is expressed as:

$$\overrightarrow{F_{\mathrm{p},\,gi}} = -\frac{1}{6}\pi {d_\mathrm{p}}^3\nabla p \tag{25}$$

where p is the gas pressure.

2.3. Model geometry and boundary conditions

For the simplicity of computation, a pseudo-two-dimensional (2D) FB model is established to investigate the effect of ultrasonic vibration on the fluidization process in the FB-ALD reactor. The model geometry is shown in figure 2(a), with the size of (3, 0.4, 20) mm. On the one hand, the width of the FB should be small enough to ensure particle flow pattern with little change along the width. On the other hand, the bed width should exceed five times of the particle diameter, making the wall effects negligible [42]. Cohesive particles are packed at the bottom of the reactor with an initial particle bed height of 2 mm. The properties of the DEM particles are set the same as that of the simple agglomerates. To avoid too much computational cost, DEM particles with a diameter of 40 μm and a density of 276 kg m^{-3} are selected in our study [43]. The Young's modulus of the DEM particles is 100 kPa and the Poisson's ratio is 0.3 [44]. Besides, the particle-to-wall and particle-to-particle friction coefficients are 0.3. The restitution coefficient is 0.9 and the rolling friction coefficient is 0.01. The background gas pressure of the FB is set at 1000 Pa, according to the reactor pressure in the high-volume particle FB-ALD process. A uniform velocity-inlet of 0.04 m s^{-1} and a pressure outlet with the gauge pressure of −200 Pa are implemented to the fluid computational domain.

Periodic motion is applied to part of the FB sidewall to investigate the effect of ultrasonic vibration on fluidization behaviors. The displacement of the vibrating wall can be described as $s = A\sin\left(2\pi f(t-t_0)\right)$, where A and f are the amplitude and frequency of ultrasonic vibration, and t_0 is the time when the ultrasonic vibration is applied to the reactor. Therefore, to simulate the effect of ultrasonic vibration on the flow field, a periodic moving boundary condition is applied to the vibrating wall of the FB using the dynamic mesh method. As shown in figure 2(b), the mesh of the fluid domain deforms periodically with the ultrasonic vibration along the x-axis. Three levels of frequencies (10, 20, 40 kHz) at the amplitude of 20 μm and three levels of amplitudes (10, 20, 30 μm) at the frequency of 20 kHz are implemented to introduce different ultrasonic vibration conditions.

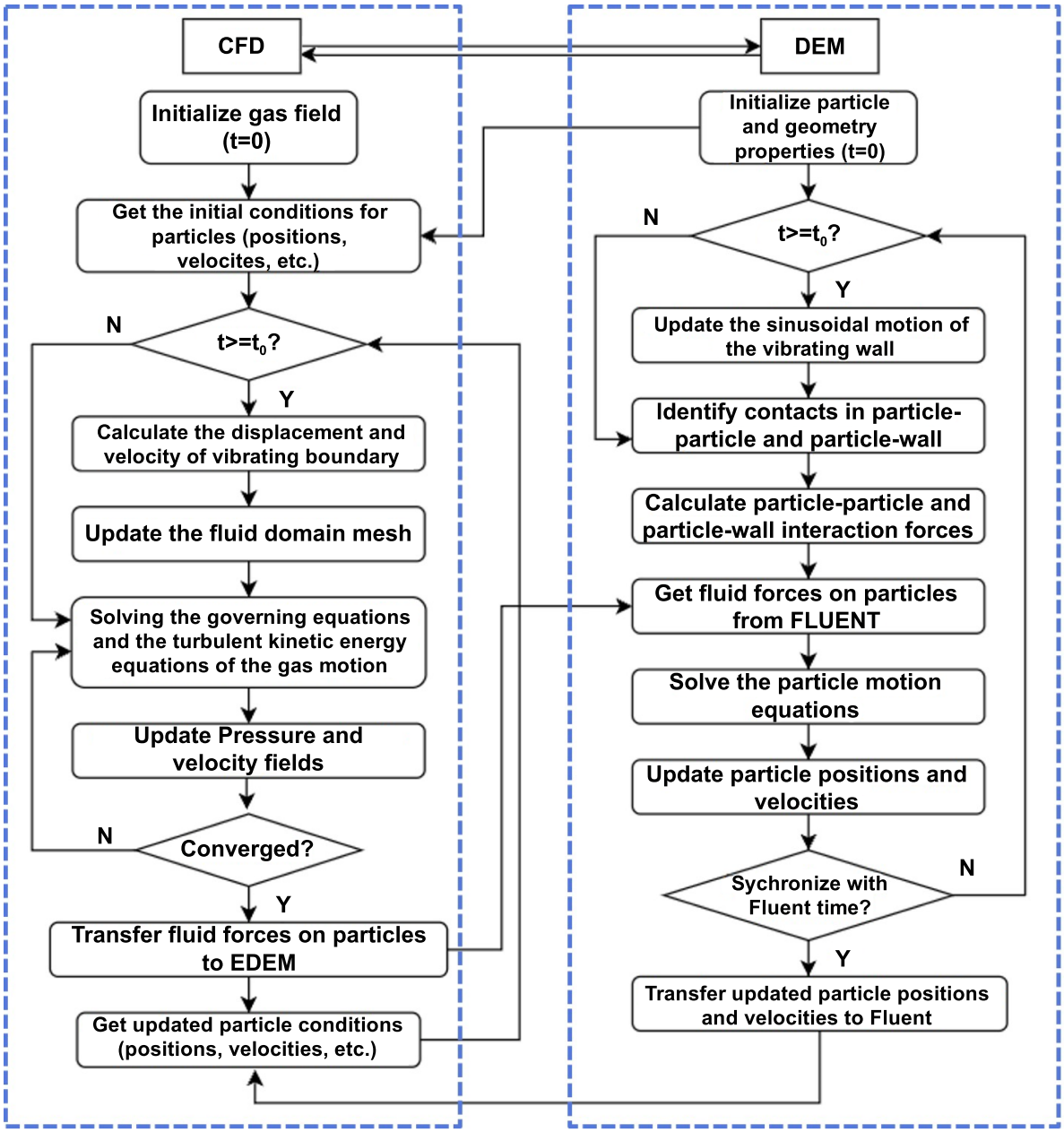

Figure 3. Flowchart of CFD-DEM coupling method.

2.4. Numerical implementation

The CFD-DEM simulations in this study are implemented in Fluent-E-discrete element method (EDEM) software with the user-defined function (UDF) and application programming interface. ANSYS Fluent 19.2 is used as the CFD solver to calculate the governing equations of hydrodynamics in the gas–solid system. The DEM code in EDEM 2020 is combined with CFD to calculate the motion of cohesive particles. The horizontal sinusoidal motion is added to the moving solid wall in EDEM, and simultaneously a UDF is implemented in Fluent to define the amplitude and frequency of ultrasonic vibration.

For the ultrasonic CFD simulation, the selection of the time step has a significant influence on the numerical results of hydrodynamics. Specifically, as the variations of the flow variables occur in the order of microseconds, the time step should be sufficiently smaller than the period of the ultrasonic wave to cover all of the oscillation characteristics [45]. As a consequence, the flow time step is set at 5×10^{-6} s for each case. DEM time step is set at 5×10^{-7} s, which is 13.9% of the Rayleigh time step. The pressure-based solver is selected for pressure–velocity coupling, and the phase coupled SIMPLE algorithm is used for the transient calculations. The absolute criteria for the convergence of continuity, velocity are set at 0.001.

2.5. CFD-DEM coupling method

Based on the above models and settings, the coupled CFD-DEM solution process for the is explained as follows in figure 3. Firstly, the initial conditions of the gas field and

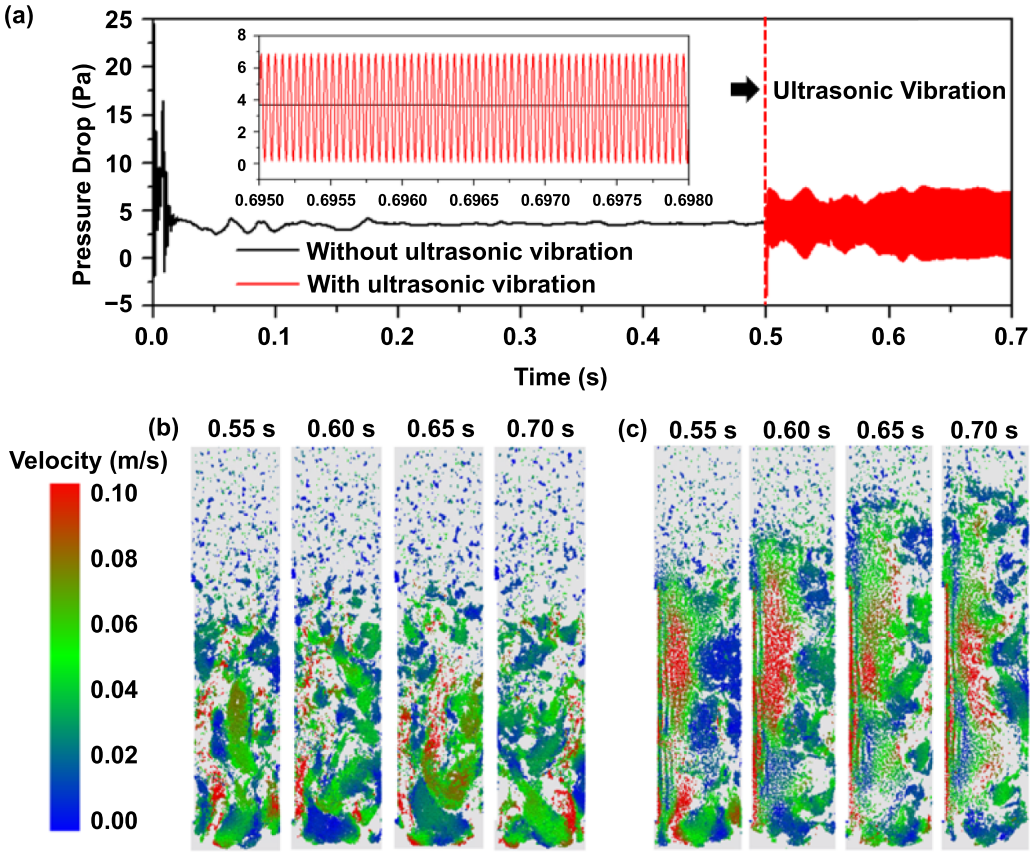

Figure 4. (a) Pressure drop versus the fluidization time for the cases of with or without ultrasonic vibration; snapshots of solids profile colored by particle velocity of (b) normal FB, and (c) ultrasonic vibration-assisted FB.

particle properties are set according to the FB-ALD deposition environment in the CFD solver and DEM code, respectively. After the initialization, the coupling process begins, enabling Fluent to get the particle properties from EDEM. DEM code calculates the particle–particle and the particle–wall interactions with the calculated wall motion. In the ultrasonic-vibration FB-ALD process, the ultrasonic vibration begins when the fluidization has already reached a steady state. Therefore, when $t < t_0$, the FB sidewall keeps static. When $t \geqslant t_0$, the UDF of the wall motion is called and the fluid domain mesh is updated. The governing equations and the turbulent kinetic energy equations of gas motion are directly solved by the CFD solver. When the solution of the governing equations and turbulent kinetics energy equations reaches convergence, the fluid forces acting on particles are transferred to EDEM. Based on the obtained volume force, the particle motions are calculated using Newton's second law and the particle positions as well as velocities are updated. After a Fluent time step, the updated particle positions and velocities are transferred into Fluent. Based on the new particle properties and new fluid domain information, the local gas volume fraction and the gas–particle interaction forces are recalculated and re-imported to the governing equations of the gas motion. Then, as similar to the above steps, the CFD solver starts a new period. Through the coupled multiscale CFD-DEM method, both the hydrodynamics of the gas and particle phases at the reactor scale and the particle agglomeration behavior at the agglomerate scale can be obtained simultaneously.

3. Results and discussions

3.1. Pressure drops and snapshots

Firstly, the pressure fluctuations and general flow patterns are presented. Pressure drops of the normal FB with an inlet gas velocity of 0.4 m s^{-1} are shown in figure 4(a). As the fluidization time increases, the pressure drop begins to reach a steady value of about 3.8 Pa. The instantaneous flow pattern of the solids is shown in figure 4(b). It is shown that the bed height of the normal FB almost remains constant from 0.55 s to 0.70 s, which indicates that the fluidization has reached a steady state. Due to the strong cohesive forces between particles, the particles are all fluidized in the form of agglomerates, leading to non-uniform dispersion of particles and obvious channeling in the normal FB. The velocity of most particles is around 0.4 m s^{-1}, while the particles with high velocities (up to 1 m s^{-1}) are distributed in the channeling areas. It is noted that particle elutriation and the gas by-passing by channeling is much unfavorable to the FB-ALD process, since it can lead to a lot of waste of both the particle materials and precursors.

In order to investigate the effect of ultrasonic vibration on the general fluidization behaviors, a typical ultrasonic vibration with a frequency of 20 kHz and an amplitude of 20 μm is applied to the FB after the fluidization reaches a steady state. For the case without ultrasonic vibration, it is shown that the pressure drop reaches a steady value of 3.8 Pa at around 0.2 s. However, when the ultrasonic vibration is implemented to the FB at 0.5 s, the pressure drop fluctuates sharply immediately. From the enlarged view of the pressure drops in figure 4(a), it is found that the amplitude of the pressure fluctuations is about 3 Pa. Besides, the frequency of the fluctuations is the same as that of the ultrasonic vibration. This indicates that the periodic intense fluctuations of the pressure signal can be attributed to the application of the external ultrasonic field, which transfers much energy into the FB. The particle flow pattern in the ultrasonic vibration-assisted FB is shown in figure 4(c). With the induce of the ultrasonic vibration, the velocity of the particles close to the vibrating wall increases up to 0.1 m s^{-1} immediately. The number of particles with high velocities also increases, leading to more particle–particle collisions. Besides, the bed height increases gradually as time increases, which implies that the ultrasonic vibration can effectively promote particle dispersion. Moreover, channeling is also reduced by the ultrasonic field. These improvements of fluidization behaviors are beneficial to the particle coating process, since the precursor molecules can diffuse faster and more uniformly into the agglomerates, thus increasing the overall coating efficiency.

3.2. *Effect of ultrasonic vibration on hydrodynamics*

In this section, the hydrodynamics of both the gas and particle phases are studied to comprehensively understand the mechanism of the ultrasonic vibration effect. Fluid turbulent motion is the primary reason for particles to achieve random motion, and turbulence kinetic energy is the key factor for evaluating the breakage energy for particle agglomerates [46]. Figure 5 is the distribution of the fluid turbulence kinetic energy with or without ultrasonic vibration along the FB length. Without the ultrasonic vibration, the turbulence kinetic energy is quite small, and it remains unchanged along the x-axis direction. However, once the ultrasonic vibration is applied, the maximum turbulence kinetic energy increases sharply. It is shown that the maximum turbulence kinetic energy increases with the frequency or amplitude increasing, and the maximum value is found to be about 200 m^2 s^{-2}, when the frequency is 20 kHz and the amplitude is 30 μm. Nevertheless, the turbulent kinetic energy also decreases rapidly along the x-axis direction due to the energy dissipation. Moreover, it is found that the ultrasonic energy with a frequency of 40 kHz decreases the fastest. The intense turbulence caused by the fluid-wall collision provides the source power of the particle disorder motion. As a consequence, the ultrasonic vibration with a frequency of 20 kHz and an amplitude of 30 μm transfers most energy into the FB-ALD system, which is bound to improve the breakage energy among the agglomerates.

As for the flow field in all FBs, the gas velocity vectors of the gas phase are shown in figure 6. Different colors are used

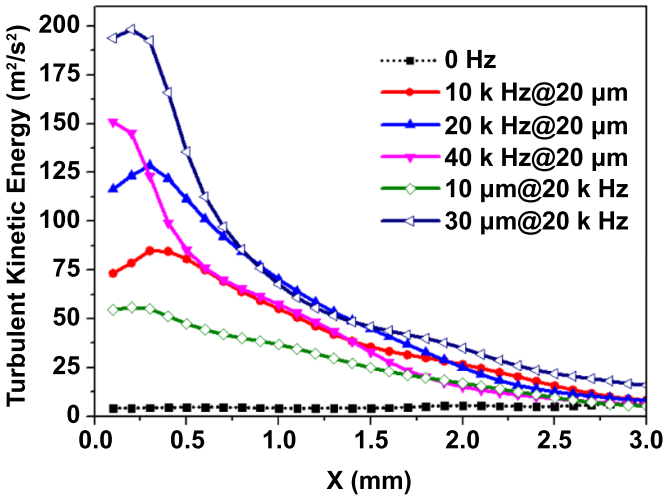

Figure 5. Distributions of fluid turbulence kinetic energy in the FB along the x-axis for all cases.

to distinguish the different gas velocity magnitudes. For the normal FB, the fluid velocity magnitude is below 0.1 m s^{-1}, and the velocity field is relatively uniform through the whole FB. As for the FBs with ultrasonic vibration, the velocity field of the gas flow becomes much uneven. More specifically, gas flow near the vibrating wall owns high velocities, with a direction of positive x-axis and values of more than 1 m s^{-1}. The gas velocity decreases along the direction of the positive x-axis, which has the same tendency of the turbulent kinetic energy. This phenomenon can be attributed to the fast dissipation of turbulence kinetic energy at high frequencies. It is shown that the area with high gas velocities increases with the amplitude increasing, and the FB with an ultrasonic vibration of 20 kHz and 30 μm owns a maximum area of gas flow with high velocities. According to equation (21), higher gas velocity will bring larger particle–fluid drag force, which improves the particle motion and promotes de-agglomeration.

In addition to the gas flow field, the effect of ultrasonic vibration on particle velocities is also examined. The average particle velocities and the distribution of particle velocities along the x-axis of the FB under different conditions are shown in figure 7. For the case without ultrasonic vibration, the distribution of average particle velocity magnitude along the x-axis is relatively uniform, fluctuating within a range from 0.02 to 0.06 m s^{-1}. However, when the ultrasonic field is applied, the average velocities of the particles close to the vibrating wall increase rapidly, due to the violent particle–wall and particle–fluid interactions. Besides, the particle velocity gradually decreases along the positive x-axis, which is similar to the tendency of the flow velocity field. It is also shown that compared to the frequency, changing the ultrasonic amplitude has a greater impact on the overall particle velocity. The maximum average particle velocity lies in the case of 20 kHz and 30 μm, with an average value of 0.05 m s^{-1} and a maximum average velocity along the x-axis of 0.17 m s^{-1}. The increasing particle velocity will definitely lead to more intensive particle–particle collisions.

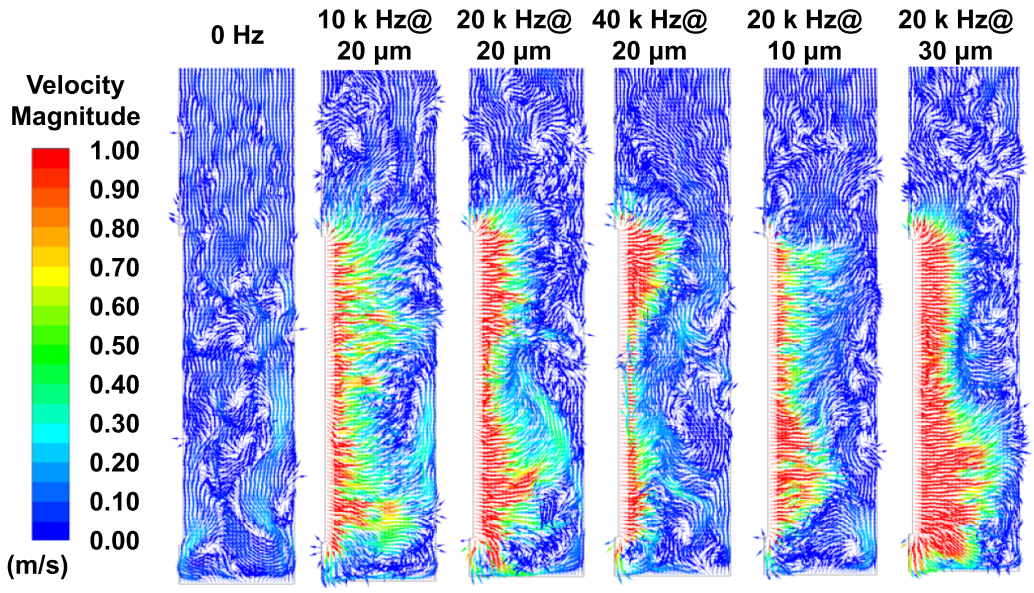

Figure 6. Gas velocity vectors in the FB for all cases.

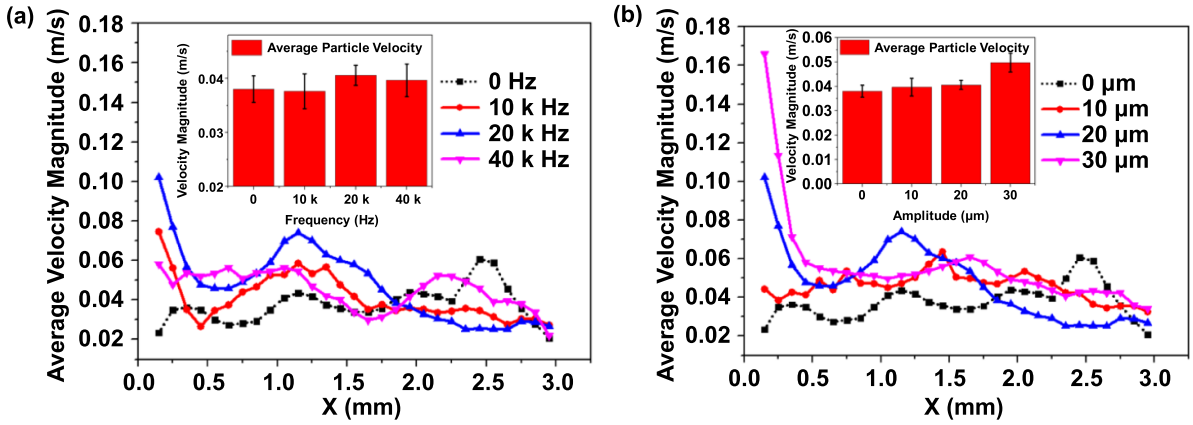

Figure 7. Average particle velocit and the distribution of particle velocities along the *x*-axis of the FB under different (a) frequencies and (b) amplitudes of ultrasonic vibration.

The distribution of solid volume fraction for different cases has been presented in figure 8, which has indicated the solid phase dispersion condition to a certain extent. As shown in figure 8(a), for the case of normal FB, the highest volume fraction reaches 0.45, and high solid concentrations can be observed through the whole bed. Besides, most of the areas with high solid volume fraction lie in the bottom region of the bed. This indicates severe agglomeration and bad dispersion of particles in the normal FB. While for the FBs with ultrasonic vibrations, the bed heights are all higher than that of the normal FB. Besides, the particle phase is more dilute and uniform in the middle area of the FB. Distribution of solid volume fraction along the *x*-axis of the FB for different frequencies and amplitudes of ultrasonic vibration has been numerically provided in figures 8(b) and (c). It is shown that when the ultrasonic vibration is applied to the FB, the average solid volume fraction decreases obviously within 0.5–2 mm from the ultrasonic vibrating wall. However, it is noted that the solid volume fraction increases abruptly within 0.3 mm from the ultrasonic wall. Besides, the higher ultrasonic frequency leads to a higher solid volume fraction in the area near the vibrating wall. This can be attributed to the agglomeration effect of the ultrasonic field, as reported in previous studies [47, 48]. According to the orthokinetic agglomeration mechanism, the differences in amplitude and speed force the agglomerates to collide and condense with each other. Comparing figure 8(b) to (c), it can be found that the agglomeration effect of ultrasonic vibration mainly depends on the ultrasonic vibrating frequency. The maximum solid volume fractions in the cases of 10 μm and 30 μm are both lower than that of the 20 μm. The reason is that the ultrasonic vibration with lower amplitudes is not intensive enough to cause agglomeration, while ultrasonic vibration with higher amplitudes leads to excess energy to disperse the aggregated particles.

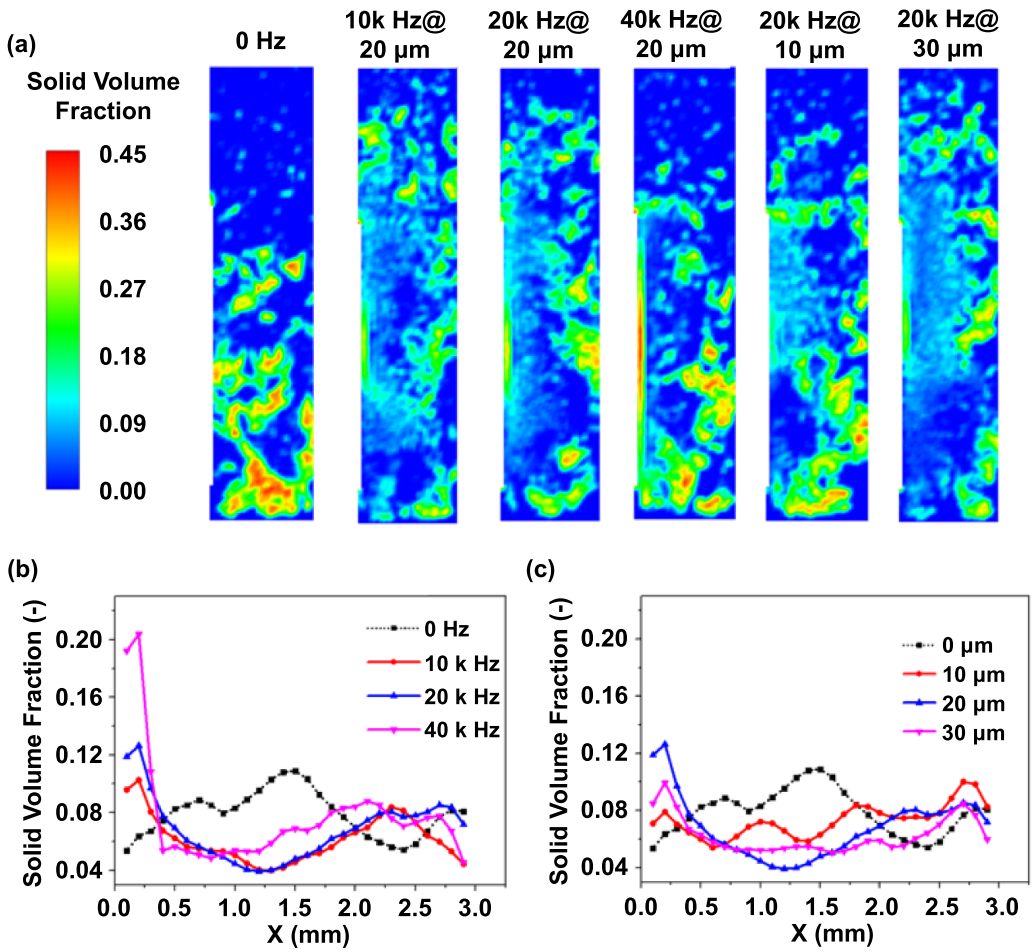

Figure 8. (a) Contours of solid volume fraction in the FB for all cases; distribution of solid volume fraction along the *x*-axis of the FB under different (b) frequencies and (c) amplitudes of ultrasonic vibration.

3.3. Effect of ultrasonic vibration on nanoparticle agglomerates

The analyses in the previous sections indicate that the ultrasonic field makes a great difference to the macro-scale hydrodynamics in the bed. In this section, changes in the agglomerate sizes will be considered for discussing the effect of ultrasonic vibration on micro-structures. The average coordination number of particles for different frequencies and amplitudes of ultrasonic vibration is shown in figure 9. It is observed in figures 9(a) and 9(b) that once the ultrasonic vibration is applied, the average particle coordination number decreases rapidly. Then, the average coordination number increases slightly and reaches a steady value at about 0.6 s. When the ultrasonic frequency is set as 10 kHz or 20 kHz, the average coordination number first decreases rapidly from 0.50 s to 0.51 s. After 0.51 s, the average coordination number of particles begins to increase. This can be attributed to the agglomeration effect of the ultrasonic vibration. The steady value of the average coordination number with the case of 40 kHz is slightly lower than that of the normal FB, which indicates that a high ultrasonic frequency of 40 kHz makes little difference to the de-agglomeration of agglomerates in the whole FB. Higher amplitudes of ultrasonic vibration lead to more decrease in the average coordination number, due to the larger breakage energy from the ultrasonic fields.

Characterizations of the coordination number and agglomerate size distribution for all cases are also carried out to quantitatively investigate the particle agglomeration and breakage behaviors, as shown in figure 10. The statistics are performed at the fluidization time of 0.7 s since the fluidization state at this time is considered relatively stable. The probabilities of coordination numbers under different cases are shown in figures 10(a) and (b). For all cases, the probability of the coordination number of 0 in the ultrasonic vibration-assisted FB is much more than that in the normal FB, indicating the effective breakage of large agglomerates by ultrasonic field. When the ultrasonic vibration with an amplitude of 10 kHz is applied to the FB, the probabilities for the average coordination number more than 3.0 decreases rapidly. At the same time, the probability for the average coordination number between 1.0 and 2.5 increases, indicating that the ultrasonic vibration with a frequency of 10 kHz can effectively break large agglomerates into small agglomerates. For the case of 20 kHz, the decrease of probabilities for the coordination number between 3 and 6, as well as a probability increase from 0.015 to 0.075 for the average coordination number of 0 indicates that the ultrasonic vibration with an amplitude of

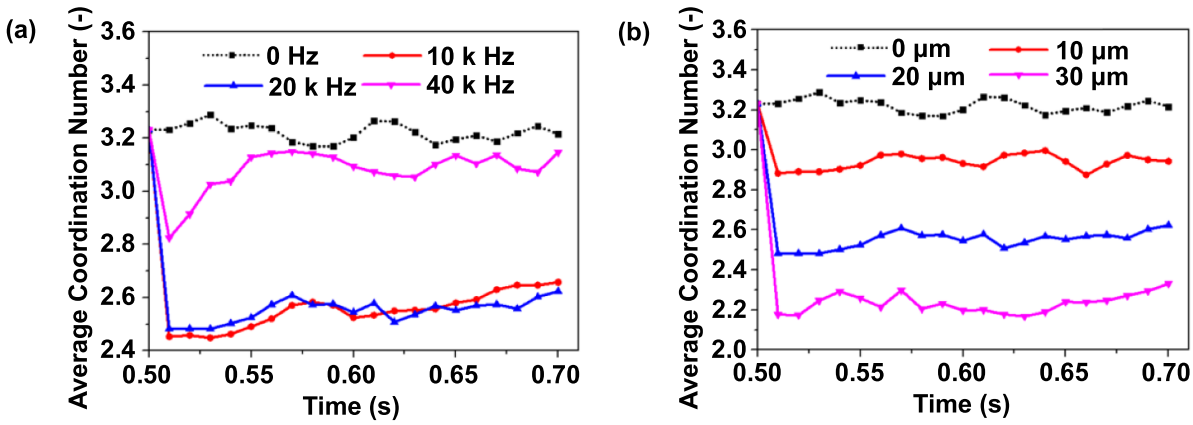

Figure 9. Average coordination number of particles under the conditions of different (a) frequencies and (b) amplitudes of ultrasonic vibration.

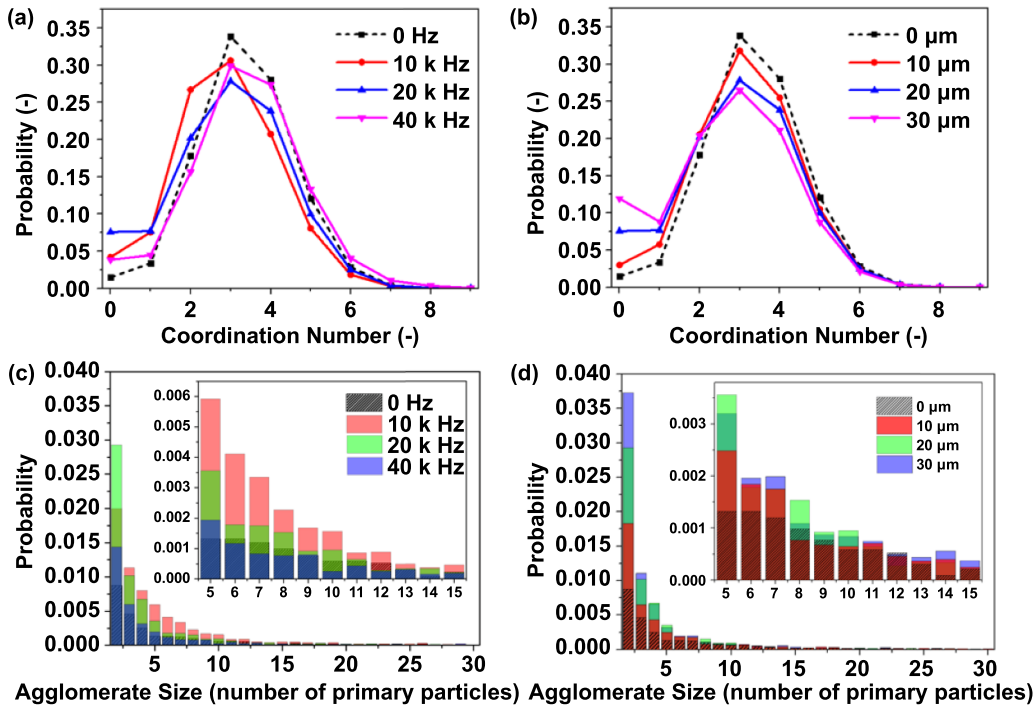

Figure 10. Probabilities of coordination number and agglomerate size under different frequencies and amplitudes of ultrasonic vibration.

20 kHz and 20 μm can effectively break the large agglomerates into small agglomerates and individual particles. However, when the ultrasonic frequency increases to 40 kHz, it is shown that although the probability for the coordination number of 0 increases from 0.015 to 0.038, the probabilities for the coordination numbers more than 4 also increase slightly. Moreover, the probability for the coordination numbers of 2 and 3 decreases from 0.051 to 0.044. This means that the ultrasonic vibration with a frequency of 40 kHz will not only lead to the de-agglomeration of agglomerates into small agglomerates or individual particles, but also cause the agglomeration of particles. When the ultrasonic frequency is set as 20 kHz, the de-agglomeration effect of the ultrasonic field increases with the ultrasonic amplitude. More specifically, the probabilities for the coordination numbers more than 3 gradually decrease, and the probabilities for the coordination numbers less than 2 gradually decrease when the amplitude of the ultrasonic vibration increases from 10 μm to 30 μm. This indicates that at the frequency of 20 kHz, the breakage instead of the agglomeration effect of ultrasonic vibration is dominant. As explained earlier, the breakage results from the enhanced particle–wall and particle–particle collisions, and the increased particle–fluid drag force by the introduced ultrasonic field.

The distributions of the agglomerate sizes in different FBs are shown in figures 10(c) and (d). Due to the strong cohesive forces between the particles, large agglomerates are formed in the normal FB, and the probability of small agglomerates formed by two primary particles is lower than 0.01.

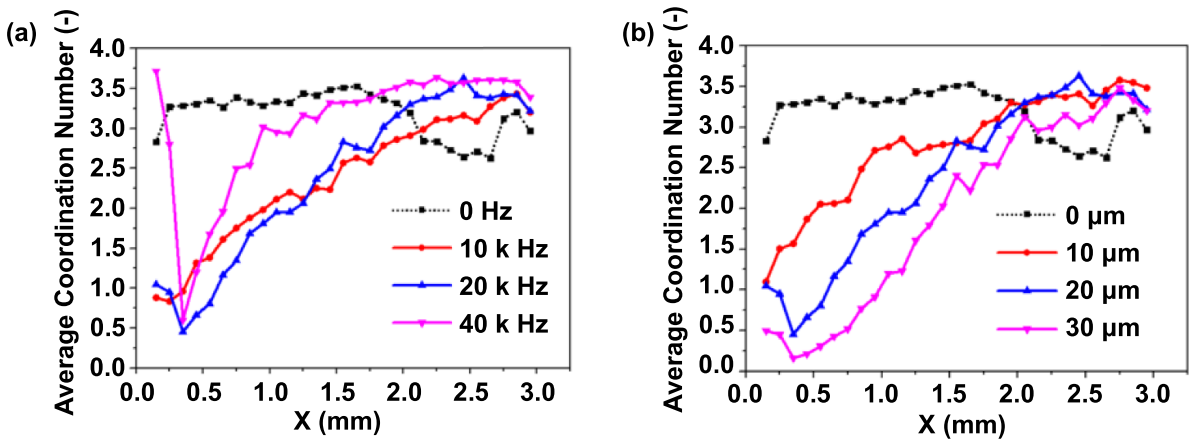

Figure 11. Distributions of average coordination number of particles along the *x*-axis under different (a) frequencies and (b) amplitudes of ultrasonic vibration.

When the ultrasonic frequency is 10 kHz, the probabilities for the agglomerates formed by two to ten primary particles all increase, which implies that the large agglomerates (formed by more than 30 primary particles) have been broken into smaller agglomerates. When the ultrasonic frequency increases from 10 kHz to 20 kHz, the probability for the agglomerates formed by two primary particles increases rapidly from 0.019 to 0.029, while the agglomerates formed by three to ten primary particles all decrease. This indicates that the ultrasonic vibration with the frequency of 20 kHz can further break the small agglomerates into the smallest agglomerate or even individual particles. However, when the ultrasonic frequency increases to 40 kHz, the probabilities for all the agglomerates formed by two to ten primary agglomerates all decrease. Therefore, the ultrasonic vibration with a frequency of 40 kHz will lead to the re-agglomeration of small agglomerates. Thus, the optimal frequency is 20 kHz, for the number of the smallest agglomerates is the highest. When the ultrasonic frequency is fixed at 20 kHz, the probabilities for the agglomerates formed by two to five primary agglomerates all increase as the amplitude increases from 10 μm to 20 μm, indicating the breakage of large agglomerates. When the ultrasonic amplitude increases to 30 μm, the probability of the smallest agglomerates further increases, which implies that the ultrasonic vibration with the frequency of 20 kHz and the amplitude of 30 μm shows the most remarkable effect for the de-agglomeration of large agglomerates.

The distribution of the average coordination number of particles along the *x*-axis for different frequencies and amplitudes of ultrasonic vibration has also been investigated. As shown in figure 11, when no external field is applied to the FB, the average coordination number is relatively uniformly distributed along the bed length, with a steady value of around 3. When the ultrasonic vibration with an amplitude of 20 μm and frequencies of 10 kHz or 20 kHz is applied to the FB, the average coordination number of the particles near the vibrating wall within 2 mm decreases rapidly. When the distance away from the ultrasonic vibrating wall exceeds 0.5 mm, the average coordination number increases with distance due to the dissipation of ultrasonic energy along the *x*-axis. As a consequence, the agglomerates mainly distribute at the right side of the FB. Nevertheless, when the ultrasonic frequency increases to 40 kHz, the average coordination number near the wall increases sharply to greater than 3.5. This can be explained by the ultrasonic agglomeration effect, which becomes stronger as the ultrasonic frequency increases, but becomes weaker as the distance from the vibration source increases. Therefore, when the ultrasonic vibration is at a frequency of 40 kHz, apart from the right side of the FB, large agglomerates also distribute near the vibrating wall. It can be concluded that there exists a critical value of the ultrasonic frequency. When the ultrasonic value is lower than the critical value, the average particle velocity and the agglomerate size increase with the ultrasonic frequency increasing. However, when the ultrasonic frequency exceeds this critical value (e.g. 40 kHz) the particles begin to agglomerate near the vibrating wall. In the ultrasonic vibration-assisted FB, the ultrasonic waves mainly propagate through the gaseous medium. When the ultrasonic frequency increases to 40 kHz, the particle agglomeration behavior near the vibrating wall is too severe, which has hindered the propagation of ultrasound in the FB. As a consequence, the particle agglomeration becomes more serious. When the ultrasonic frequency is fixed at 20 kHz, the average agglomerate size decreases as the amplitude increases. As for the cases in which the vibration frequency is fixed at 20 kHz, and the amplitude varies from 10 μm to 30 μm, large agglomerates mainly distribute at the right side of the FB. Moreover, as the amplitude increases, the agglomerate size near the vibrating wall becomes much smaller. Since the particles in the FB are in a circulating state, when the agglomerates are circulated to the area near the vibrating wall, ultrasonic vibration with a frequency of 20 kHz and an amplitude of 30 μm is the most effective for breaking the agglomerates.

In the high-volume ultrasonic vibration-assisted FB-ALD manufacturing process, particles experience fluctuating stresses, leading to both aggregation and breakage of agglomerates. The selections of the ultrasonic frequencies or amplitudes depends on many factors, such as the reactor pressure, the equivalent inter-particle cohesive forces, as well as the particle size distribution in the whole FB. Knoop *et al* have

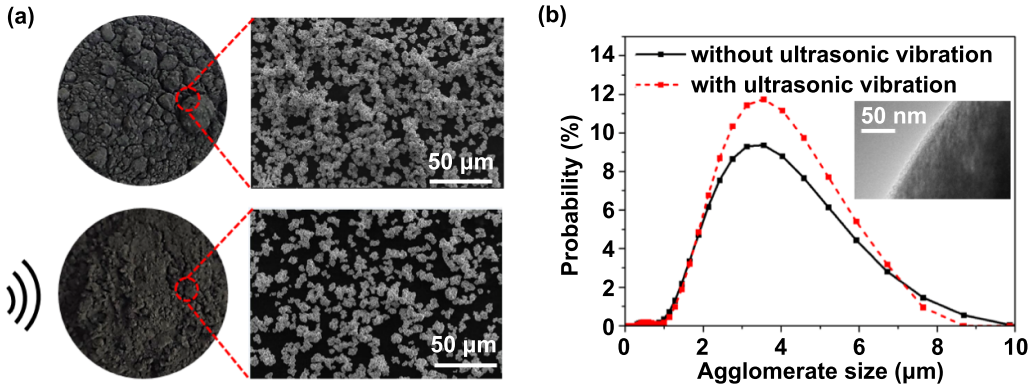

Figure 12. (a) The morphology and SEM images of the nanoparticles after coating using normal FB-ALD reactor and ultrasonic vibration-assisted FB-ALD reactor; (b) agglomerate size distribution of coated NCM811 nanoparticles using FB-ALD with and without ultrasonic vibration and a TEM image of the NCM811 particle coated with 50 cycles of Al_2O_3 with ultrasonic assistance.

found that an increase in primary particle size or density leads to a decrease in the ultrasonic power needed to achieve a certain probability of breakage, due to the decreased equivalent cohesive force. In contrast, an increase in relative humidity requires higher specific breakage energy [49]. Moreover, the inner structure of the FB-ALD rector and the installation position or number of the ultrasound sources onto the reactor wall also play important roles in the hydrodynamics of the gas–solid flow, thus influencing the agglomeration behavior at the micro-scale and the deposition behaviors at the atomic-scale. Due to the inconsistent distribution of fluidization mass in the height direction of the FB, it may be necessary to arrange ultrasonic wave sources with different ultrasonic frequencies and amplitudes at different locations. For the optimal design of the ultrasonic vibration-assisted FB-ALD reactor, knowledge from adjacent fields such as hydromechanics and mechanical engineering is further required.

4. Experimental verification

To verify the simulation results, comparative coating experiments have been performed with ultrasonic vibration-assisted FB-ALD reactor on $LiNi_{0.8}Co_{0.1}Mn_{0.1}O_2$ (NCM811, purchased from Shenzhen Kejing Star Technology Company) particles, which can offer high energy density in automotive lithium-ion batteries (LIBs) [50]. The coating process is performed in a homemade ultrasonic vibration-assisted FB-ALD reactor for surface coating of NCM811 nanoparticles. TMA and H_2O are selected as the organometallic precursor and the oxidant to fabricate Al_2O_3 films. An ultrasonic transducer is connected to the sidewall of the FB-ALD reactor to induce ultrasonic waves. During the assistance of ultrasonic vibration, the ultrasonic frequency is set at 19.59 kHz. About 100 g NCM811 nanoparticles are loaded in the designed powder holder with the top and bottom being sealed by a stainless-steel screen. In each half-reaction, the precursor molecules are carried by N_2 into the bottom of the FB. After each reactant dose, the system is purged with N_2 to eliminate the unreacted precursors as well as the byproducts. The coating process proceeds at the temperature of 150 °C. One ALD cycle for Al_2O_3 consists of the following four steps: (a) a 600 s pulse of TMA precursor, (b) a purging time of 800 s, (c) a 600 s pulse of H_2O precursor, and (d) a purging time of 1000 s.

The morphology and SEM (Quanta 200) images of the NCM811 nanoparticles after coating using normal FB-ALD reactor and ultrasonic vibration-assisted FB-ALD reactor are shown in figure 12(a). For the case of the normal FB-ALD reactor, large agglomerates are found in the morphology image, leading to a very rough surface. In contrast, the agglomerates of nanoparticles coated by ultrasonic vibration-assisted FB-ALD reactor are much smaller. This phenomenon indicates that the ultrasonic field has led to effective breakage of large agglomerates. The SEM images of the coated nanoparticles also show that, compared to the severe agglomeration in the normal FB-ALD reactor, the particles in the ultrasonic vibration-assisted FB-ALD have been effectively dispersed, which is favorable to the full contact between precursor molecules and the nanoparticle surfaces, leading to more conformal layers and a higher coating efficiency.

The agglomerate size distribution of coated NCM811 nanoparticles is shown in figure 12(b). Due to the strong cohesive forces between nanoparticles, the agglomerate sizes of NCM811 are concentrated between 2 and 7 μm. Compared to the case without ultrasonic vibration, the probabilities of the agglomerates with the size between 2 and 7 μm increase a lot, and the probabilities of large agglomerates with the size from 7 to 10 μm all decrease. This has demonstrated that the ultrasonic vibration can effectively break the large agglomerates in the FB-ALD reactor, leading to a more uniform distribution of precursors on particle surfaces. The experimental data also agree well with the simulation results shown in figure 10, which has verified the effectiveness of the dynamic multiscale CFD-DEM model. To clearly show the ALD coating on the particle surface with ultrasonic assistance, a TEM characterization of the NCM811 particles coated with 50 cycles of Al_2O_3 is performed. As shown in figure 12(b), a uniform layer is

coated on the particle with a thickness of 8.0 nm. The film growth rate is 1.6 Å/cycle, which is within the normal range of ALD growth. The initial capacity of the button half-cells of the NCM811 material coated with 0.2 nm Al_2O_3 layer by ultrasonic vibration-assisted FB-ALD is basically the same as that of uncoated particles, which is about 210 mAh g^{-1} (under the test condition of 3–4.7 V, 0.2 °C). This indicates that ultrasound-assisted FB-ALD achieves uniform particle dispersion and conformal atomic-level coating on individual particles. Both the simulation and experimental results have proved that ultrasonic vibration-assisted FB-ALD reactor is a promising manufacturing method for the mass production of nanoparticle coatings, especially for the surface modification of high-volume LIB cathode materials.

5. Conclusion

In this study, the effects of ultrasonic vibration on the nanoparticle fluidization behaviors in the atomic coating process are numerically investigated via a multiscale modeling and experimental study. Simulations are performed with different frequencies (10 kHz, 20 kHz, and 40 kHz) and amplitudes (10 μm, 20 μm, and 30 μm). It is found that the ultrasonic vibration can effectively increase the bed height, promoting the solids dispersion as well as the agglomerate breakage near the vibrating wall. Experimental results have also demonstrated that better fluidization quality and higher coating efficiency can be obtained in the ultrasonic vibration-assisted FB-ALD reactor.

It is expected that various kinds of particulate materials are going to benefit a lot from the ultrasonic vibration-assisted FB-ALD technology. Compared to the normal FB-ALD process, the assistance of ultrasonic vibration can effectively accelerate the velocity of fluid and particles near the vibrating wall. This leads to much more violent particle–particle collisions and larger particle–fluid drag force, resulting in the decrease of agglomerate size and improvement of the particle dispersion. Enhanced fluidization quality of nanoparticles is also bound to facilitate the heat transfer and precursor diffusion in the whole FB-ALD reactor and the agglomerates, which can largely shorten the coating time and improve the film conformality as well as precursor utilization.

For the scale-up of ultrasonic vibration-assisted FB-ALD system, a multiscale model with the consideration of the macro-scale reactor, meso-scale particle structures and micromechanics is of great importance. Although the current multiscale CFD-DEM model covers scales only from the simple agglomerates to the FB with a size of a few millimeters, it has successfully revealed the particle agglomeration and breakage behaviors with ultrasonic assistance. With the development of the multiscale theory and computational science, this model is believed to be further developed for a better investigation from lab-scale to manufacturing-scale. It can also provide numerous guidance to the process optimization as well as the reactor design for the atomic-scale manufacturing of high-volume particle coating, thus broadening their various commercial applications.

Acknowledgments

This work is supported by the National Natural Science Foundation of China (51835005 and 51911540476), National Key Research and Development Program of China (2020YFB2010401), Hubei Province Natural Science Foundation for innovative research groups (2020CFA030), Independent Innovation Research Fund of HUST (2019kfyXMBZ025), and Tencent Foundation. Lijie Li would like to acknowledge the Engineering and Physical Sciences Research Council project (EP/T019085/1). The authors would also like to acknowledge Yuanxiao Chen for writing the code of agglomerate characterization. The authors would like to acknowledge the technology support by the Flexible Electronics Research Center of HUST & Analytic Testing Center of HUST.

Conflict of interest

We declare that we have no conflict of interest.

ORCID iDs

Lijie Li https://orcid.org/0000-0003-4630-7692
Rong Chen https://orcid.org/0000-0001-7371-1338

References

[1] Cao Y Q, Meng X B and Li A D 2021 Atomic layer deposition of high-capacity anodes for next-generation lithium-ion batteries and beyond *Energy Environ. Mater.* **4** 363–91
[2] Xiong Q G, Hajjar A, Alshuraiaan B, Izadi M, Altnji S and Shehzad S A 2021 State-of-the-art review of nanofluids in solar collectors: a review based on the type of the dispersed nanoparticles *J. Clean. Prod.* **310** 127528
[3] Sun Q, Lau K C, Geng D S and Meng X B 2018 Atomic and molecular layer deposition for superior lithium-sulfur batteries: strategies, performance, and mechanisms *Batter. Supercaps* **1** 41–68
[4] Zhang S F, Zhang B, Liang H J, Liu Y Q, Qiao Y and Qin Y 2018 Encapsulation of homogeneous catalysts in mesoporous materials using diffusion-limited atomic layer deposition *Angew. Chem., Int. Ed.* **130** 1103–7
[5] Yang J F, Cao K, Gong M, Shan B and Chen R 2020 Atomically decorating of MnO_x on palladium nanoparticles towards selective oxidation of benzyl alcohol with high yield *J. Catal.* **386** 60–69
[6] Li S, Xiong J X, Shen J S, Qin Y, Li J, Chu F Q, Kong Y and Deng L H 2015 A novel hydrogen peroxide sensor based on Ag nanoparticles decorated polyaniline/graphene composites *J. Appl. Polym. Sci.* **132** 42409
[7] Cao K, Cai J M, Shan B and Chen R 2020 Surface functionalization on nanoparticles via atomic layer deposition *Sci. Bull.* **65** 678–88
[8] Fang F Z 2020 Atomic and close-to-atomic scale manufacturing: perspectives and measures *Int. J. Extrem. Manuf.* **2** 030201

[9] Fang F *et al* 2020 Atomic layer deposition assisted encapsulation of quantum dot luminescent microspheres toward display applications *Adv. Opt. Mater.* **8** 1902118

[10] Chen R, Li Y C, Cai J M, Cao K and Lee H B R 2020 Atomic level deposition to extend Moore's law and beyond *Int. J. Extrem. Manuf.* **2** 022002

[11] George S M 2010 Atomic layer deposition: an overview *Chem. Rev.* **110** 111–31

[12] Muñoz-Rojas D, Maindron T, Esteve A, Piallat F, Kools J C S and Decams J M 2019 Speeding up the unique assets of atomic layer deposition *Mater. Today Chem.* **12** 96–120

[13] van Ommen J R, Valverde J M and Pfeffer R 2012 Fluidization of nanopowders: a review *J. Nanopart. Res.* **14** 737

[14] Shabanian J, Jafari R and Chaouki J 2012 Fluidization of ultrafine powders *Int. Rev. Chem. Eng.* **4** 16–50

[15] Zhu X L, Zhang Q, Wang Y and Wei F 2016 Review on the nanoparticle fluidization science and technology *Chin. J. Chem. Eng.* **24** 9–22

[16] Li Z S, Li J W, Liu X and Chen R 2021 Progress in enhanced fluidization process for particle coating via atomic layer deposition *Chem. Eng. Process. Process Intensif.* **159** 108234

[17] van Ommen J R, Grillo F and Grievink J 2019 Scalable manufacturing of nanostructured materials by atomic layer deposition in fluidized bed reactors *Comput. Aided Chem. Eng.* **46** 403–8

[18] van Ommen J R and Goulas A 2019 Atomic layer deposition on particulate materials *Mater. Today Chem.* **14** 100183

[19] Hakim L F, Blackson J, George S M and Weimer A W 2005 Nanocoating individual silica nanoparticles by atomic layer deposition in a fluidized bed reactor *Chem. Vapor Depos.* **11** 420–5

[20] King D M, Spencer I I J A, Liang X H, Hakim L F and Weimer A W 2007 Atomic layer deposition on particles using a fluidized bed reactor with *in situ* mass spectrometry *Surf. Coat. Technol.* **201** 9163–71

[21] Tiznado H, Domínguez D, Muñoz-Muñoz F, Romo-Herrera J, Machorro R, Contreras O E and Soto G 2014 Pulsed-bed atomic layer deposition setup for powder coating *Powder Technol.* **267** 201–7

[22] Duan C L, Deng Z, Cao K, Yin H F, Shan B and Chen R 2016 Surface passivation of Fe_3O_4 nanoparticles with Al_2O_3 via atomic layer deposition in a rotating fluidized bed reactor *J. Vac. Sci. Technol.* A **34** 04C103

[23] Barletta D, Donsì G, Ferrari G, Poletto M and Russo P 2008 The effect of mechanical vibration on gas fluidization of a fine aeratable powder *Chem. Eng. Res. Des.* **86** 359–69

[24] Park S W, Kim J W, Choi H J and Shim J H 2014 Vibration atomic layer deposition for conformal nanoparticle coating *J. Vac. Sci. Technol.* A **32** 01A115

[25] Jin W J, van Ommen J R and Kleijn C R 2019 Moving reaction fronts in fractal nanoparticle agglomerates *Chem. Eng. Sci.* **206** 180–6

[26] van der Hoef M A, van Sint Annaland M, Deen N G and Kuipers J A M 2008 Numerical simulation of dense gas-solid fluidized beds: a multiscale modeling strategy *Annu. Rev. Fluid Mech.* **40** 47–70

[27] Duan C L, Zhu P H, Deng Z, Li Y, Shan B, Fang H S, Feng G and Chen R 2017 Mechanistic modeling study of atomic layer deposition process optimization in a fluidized bed reactor *J. Vac. Sci. Technol.* A **35** 01B102

[28] Wang S Y, Chen Y J, Jia Y B, Tian R C, Sun Q J, Fan J W and Ma Y M 2018 Numerical simulation of flow behavior of particles in a gas-solid stirred fluidized bed *Powder Technol.* **338** 119–28

[29] Kawaguchi T, Tanaka T and Tsuji Y 1998 Numerical simulation of two-dimensional fluidized beds using the discrete element method (comparison between the two- and three-dimensional models) *Powder Technol.* **96** 129–38

[30] Wu Y, Liu D Y, Ma J L and Chen X P 2018 Effects of gas-solid drag model on Eulerian–Eulerian CFD simulation of coal combustion in a circulating fluidized bed *Powder Technol.* **324** 48–61

[31] Zhong H B, Zhang Y N, Xiong Q G, Zhang J T, Zhu Y Q, Liang S R, Niu B and Zhang X Y 2020 Two-fluid modeling of a wet spouted fluidized bed with wet restitution coefficient model *Powder Technol.* **364** 363–72

[32] Rossbach V, Padoin N, Meier H F and Soares C 2021 Influence of ultrasonic waves on the gas-solid flow and the solids dispersion in a CFB riser: numerical and experimental study *Powder Technol.* **389** 430–49

[33] Rossbach V, Padoin N, Meier H F and Soares C 2020 Influence of acoustic waves on the solids dispersion in a gas-solid CFB riser: numerical analysis *Powder Technol.* **359** 292–304

[34] Namdarkedenji R, Hashemnia K and Emdad H 2018 Effect of flow pulsation on fluidization degree of gas-solid fluidized beds by using coupled CFD-DEM *Adv. Powder Technol.* **29** 3527–41

[35] Zhang Y, Jia Y, Xu J, Wang J W, Duan C L, Ge W and Zhao Y M 2020 CFD intensification of coal beneficiation process in gas-solid fluidized beds *Chem. Eng. Process. Process Intensif.* **148** 107825

[36] Liu D Y, van Wachem B G M, Mudde R F, Chen X P and van Ommen J R 2016 An adhesive CFD-DEM model for simulating nanoparticle agglomerate fluidization *AIChE J.* **62** 2259–70

[37] Zhu L and Tang Y 2020 Effects of acoustic fields on the dynamics of micron-sized particles in a fluidized bed *Powder Technol.* **372** 625–37

[38] Rahimi M, Shahhosseini S and Movahedirad S 2019 Hydrodynamic and mass transfer investigation of oxidative desulfurization of a model fuel using an ultrasound horn reactor *Ultrason. Sonochem.* **52** 77–87

[39] Liu R, Liu Y and Liu C Z 2013 Development of an efficient CFD-simulation method to optimize the structure parameters of an airlift sonobioreactor *Chem. Eng. Res. Des.* **91** 211–20

[40] Khadilkar A, Rozelle P L and Pisupati S V 2014 Models of agglomerate growth in fluidized bed reactors: critical review, status and applications *Powder Technol.* **264** 216–28

[41] Liu D Y, Wang Z, Chen X P and Liu M L 2018 Simulation of agglomerate breakage and restructuring in shear flows: coupled effects of shear gradient, surface energy and initial structure *Powder Technol.* **336** 102–11

[42] Zhao X L, Li S Q, Liu G Q, Yao Q and Marshall J S 2008 DEM simulation of the particle dynamics in two-dimensional spouted beds *Powder Technol.* **184** 205–13

[43] de Martín L and van Ommen J R 2013 A model to estimate the size of nanoparticle agglomerates in gas-solid fluidized beds *J. Nanopart. Res.* **15** 2055

[44] Fabre A, Salameh S, Ciacchi L C, Kreutzer M T and van Ommen J R 2016 Contact mechanics of highly porous oxide nanoparticle agglomerates *J. Nanopart. Res.* **18** 200

[45] Rahimi M, Movahedirad S and Shahhosseini S 2017 CFD study of the flow pattern in an ultrasonic horn reactor: introducing a realistic vibrating boundary condition *Ultrason. Sonochem.* **35** 359–74

[46] Ge J Q, Ren Y L, Xu X S, Li C, Li Z A and Xiang W F 2021 Numerical and experimental study on the ultrasonic-assisted soft abrasive flow polishing characteristics *Int. J. Adv. Manuf. Technol.* **112** 3215–33

[47] de Sarabia E R F, Gallego-Juárez J A, Rodríguez-Corral G, Elvira-Segura L and González-Gómez I 2000 Application of high-power ultrasound to enhance fluid/solid particle separation processes *Ultrasonics* **38** 642–6

[48] Shi Y, Wei J H, Qiu J, Chu H B, Bai W W and Wang G Q 2020 Numerical study of acoustic agglomeration process of

droplet aerosol using a three-dimensional CFD-DEM coupled model *Powder Technol.* **362** 37–53

[49] Knoop C, Todorova Z, Tomas J and Fritsching U 2016 Agglomerate fragmentation in high-intensity acoustic standing wave fields *Powder Technol.* **291** 214–22

[50] Ramasamy H V, Sinha S, Park J, Gong M, Aravindan V, Heo J and Lee Y S 2019 Enhancement of electrochemical activity of Ni-rich $LiNi_{0.8}Mn_{0.1}Co_{0.1}O_2$ by precisely controlled Al_2O_3 nanocoatings via atomic layer deposition *J. Electrochem. Sci. Technol.* **10** 196–205